

Sub-wavelength gratings-based architectures through the CMOS fabrication process

Enxiao Luan*

*Department of Electrical and Computer Engineering, The University of British Columbia,
2332 Main Mall, Vancouver, BC. V6T 1Z4, Canada

1. ABSTRACT

In this work, we designed and fabricated the state-of-the-art silicon photonic-based configuration through CMOS fabrication processes, namely, sub-wavelength gratings (SWG). Due to the fabrication limitations of the 193 nm deep-UV lithography technique, the SWG-based configuration has a large low-index gap between each silicon pillar, which makes it difficult to maintain the Floquet-Bloch mode propagating in the waveguide with low losses. A litho-simulation custom software was employed to simulate UV-lithography effects on the proposed SWG geometry. Two CMOS foundries are involved in this research for device fabrication. Simulation results according to Lumerical MODE and FDTD Solutions, as well as real optical measurements from the IME-fabricated chips, are presented for the proposed SWG waveguide-based architectures, presenting huge optical losses in the resonator-based architecture with a quality factor around 450. In addition, the propagation losses and the crosstalk of SWG-based waveguides and crossings are also characterized through devices from the AMF foundry. Experimental results indicate that the propagation losses of the SWG waveguide is around 37 dB/cm, and the crosstalk of the SWG crossing is lower than -40 dB.

2. INTRODUCTION

Silicon photonics is a promising technology that can be used to integrate high-density photonic integrated circuits (PICs) into a single package for high-speed and power-efficient telecommunications. Due to its CMOS foundry processes compatibility, most silicon PICs can be manufactured with a low cost at high volume,¹ which makes photonics to be an important role in next-generation data centers, high-performance computing, and integrated components for communication technologies. Not only in the field of data communication, but biosensors based on silicon PICs have also attracted growing interest over the last decade. These optical biosensors use near-infrared light confined to silicon waveguides to sense the capture of molecules at the waveguide surface. Leveraging the CMOS fabs, silicon photonic biosensors show the possibility to integrate the light source, sensor, and readout components on a single substrate as a portable lab-on-a-chip (LOC) system with high multiplexity, which well matches the contemporary needs of the point-of-care (POC) and home healthcare diagnosis.

Sub-wavelength grating (SWG) has been considered as a novel and promising metamaterial since the first demonstrations by the National Research Council of Canada (NRC) in 2006.² By periodically interleaving the silicon core with low index materials, an SWG waveguide is formed with a period (Λ) far smaller than the wavelength (λ) of the light. Due to its unique geometry, the SWG waveguide supports a largely extended optical mode: the Floquet-Bloch (FB) mode, in which reflection and diffraction effects are suppressed.³ SWG-based structures have been investigated in many optical configurations, such as the subwavelength-engineered edge couplers,⁴ surface grating couplers hybridized with optical metasurfaces,⁵ the broad-band polarization-independent directional couplers,⁶ as well as evanescent field-based sensors.⁷ It has been theoretically⁷ and experimentally⁸ demonstrated that SWG-based planar sensing devices had enhanced sensor performance, presenting a bulk sensitivity (S_{bulk}) over 400 nm/RIU (nanometer per refractive index unit). However, almost all SWG-based configurations were fabricated through the electron-beam lithography (EBL) process, a rapid prototyping method as an alternative and complement to what is available via 193 nm deep-UV lithography-based foundries. Due to its electron beam lithography-based technique, EBL offers a much smaller fabrication minimum feature size, but is more expensive

This work is dedicated to CMC SiEPIC Silicon Passives Course and Workshop 2016, at Laval University
E. Luan: E-mail: eluan@ece.ubc.ca, Telephone: +1-778-952-8807

and time-consuming with low-yield compared to CMOS processes. Therefore, it is meaningful and trending to implement SWG-based configuration manufacturing through CMOS fabs to migrate novel configurations into cheaper, faster manufacturing systems and extend their applications.

In this paper, we designed and characterized silicon photonic-based architectures by using SWG geometries following the design rules of deep-UV lithography-based foundries, i.e., Institute of Microelectronics (IME) and Advanced Micro Foundry (AMF), at Singapore. Two kinds of SWG-based devices were employed for the proposed SWG geometry: the microring resonator (MRR), and the waveguide crossing. Due to the fabrication limitations, the minimum feature sizes that IME and AMF foundries offer are 180 nm and 120 nm, respectively, which makes it tricky to confine the FB mode in the SWG waveguide and generates more losses. By employing IME-based lithography simulations, a kind-of-real fabricated SWG-based configuration was observed according to CMOS processes, which can be applied to predict and optimize the device optical performance. The lithography simulation shows that the sub-wavelength silicon pillar is round-cornered and smaller compared to the layout, due to the lithography effect, which reduces the effective index (n_{eff}) and causes more substrate leakage. Experimental results of the IME-fabricated SWG-based MRR indicate a low Q -factor around 450, with the SWG period of 300 nm. To improve the optical performance of the proposed SWG geometry, a trapezoidal-shape SWG block was introduced to minimize the bend losses in the MRR. Instead of using the deep-UV lithography technique, which requires a long turn-around time, we employed the EBL process as a rapid prototyping for the trapezoidal-shape SWG waveguide (IME lithography effect included), presenting an improved quality factor of 10400 with the extinction ratio of 30 dB, indicating the potential of manufacturing SWG-based architectures through CMOS fabs. In addition, waveguide crossings were also realized by using the SWG geometry. By designing the SWG crossing with a period of 240 nm and a duty cycle of 50%, an AMF-fabricated crossing was achieved with the oxide cladding, showing a crosstalk of lower than -40 dB. The propagation losses of the proposed SWG waveguide were characterized by using the symmetric MZI architecture, showing the α^{SWG} of 37 dB/cm.

3. PROPOSED DESIGNS

Similarly to Bragg gratings, SWG configurations also consist of the periodic structure of their waveguide core. However the period (Λ) of SWGs is much smaller than the Bragg condition in order to maintain the propagation mode in the waveguide with no loss, i.e., $\Lambda \ll \lambda/(2n_{\text{eff}})$, where n_{eff} is the effective index. Due to the material dispersion, with the decrease of the optical wavelength, the effective index of the waveguide increases. Therefore, a smaller period is required in order to obtain the FB mode in the SWG waveguide. For the EBL fabrications, due to the ultra-fine pattern writing by the electron beam, the minimum feature size of silicon from Ebeam-based process design kits (PDK) can be reduced to 40–60 nm, which offer a wide-wavelength-supportable SWG geometry. However, as for CMOS fabrications, the minimum feature size from SiEPIC IME-based PDK is 180 nm or 120 nm for both silicon and gap with oxide cladding for IME and AMF, respectively, which limits the possibility for the design of SWG waveguides.

To characterize the optical performance of SWG-based devices fabricated by CMOS facilities, a finely designed SWG configuration is needed at a higher wavelength, i.e., C-band wavelengths, which can slightly free the period limitation. The effective index of the SWG-based waveguide is simulated by employing Lumerical Solutions. Instead of using the most rigorous full-3D vectorial Finite-Difference-Time-Domain (FDTD) approach, which is very time-consuming,⁸ an alternative is employed to simulate a single unit cell using Bloch boundary conditions in the propagation direction, which has already been applied to simulate SWG and Bragg waveguides.^{8,9} By using this approach, an infinitely long waveguide can be studied effectively without considering the whole structure (presented in Figure 1(a)). Figure 1(b) shows the simulated effective index of SWG waveguides with varied SWG period from 300 to 400 nm under water and oxide claddings, respectively, where the duty cycle (η) is fixed as 0.5. To make sure that the SWG waveguide supports the FB mode constantly in the C-band, all the simulations were carried out at the wavelength of 1500 nm, where the cutoff index has the minimum value (n_{eff} below the cutoff can maintain the FB mode).

To minimize the Bragg reflection effect, we finally chose the SWG waveguide with the following parameters: $\Lambda = 300$, $\eta = 0.5$ for the SWG waveguide-based configurations fabrication through the IME foundry (slightly breaks the design rules of 180 nm); and $\Lambda = 240$, $\eta = 0.5$ through the AMF foundry. The microring resonator (MRR) is selected as the performance characterization architecture for the IME-based tapeout since the optical spectrum

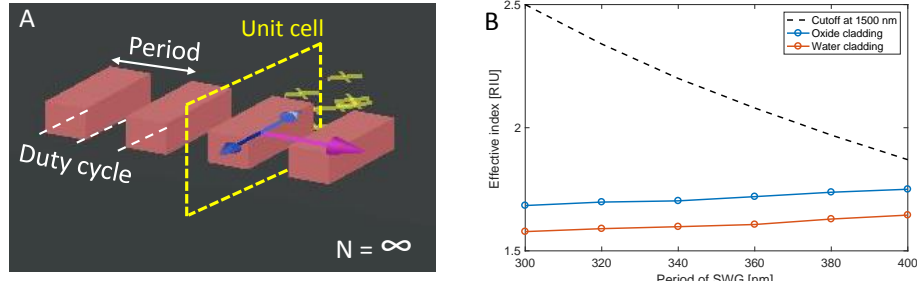


Figure 1: (a) Schematic of the SWG waveguide with 4 periodic units from FDTD Solutions. Period equals the total length of silicon and gap in one unit. Duty cycle is the length ratio of silicon and gap. For the band structure-based simulation, the length of the waveguide is infinite. (b) Simulated effective index of the SWG-based waveguide as a function of the SWG period from 300 to 400 nm, where the duty cycle is 0.5, at 1500 nm wavelengths and in the TE mode. A cutoff index boundary, generated from the Bragg condition based on each period, is also presented, under which the FB mode is supported in the SWG waveguide.

of an MRR is well-studied and can offer plenty of optical information, such as the group index, propagation losses, coupling coefficient, etc. As for the AMF tapeout, since it offers a smaller feature size, we employed the SWG-based waveguide crossing to investigate its applications. Furthermore, a series of cut-back SWG waveguides with different lengths were also designed on the AMF tapeout to characterize its propagation performance.

4. DESIGN MODELLING

4.1 Modelling of SWG-based architectures

4.1.1 Microring resonators

In this part, the SWG waveguide-based MRR configuration is designed and optimized according to the simulations. For an MRR devices, one of the important figure of merits is the quality factor (Q -factor). Q -factor describes the photon lifetime in the resonator before the energy has decayed to 37% of the initial energy, which incorporates total distributed losses of a resonator.¹⁰ From Fabry-Perot resonator theory, the inverse of the total Q -factor equals the sum of all contributing Q -factors.¹¹ In the case of the MRR, there are two loss mechanisms determine the Q -factor: the coupling loss and the waveguide loss; thus the total Q -factor can be written as:¹²

$$\frac{1}{Q} = \frac{1}{Q_c} + \frac{1}{Q_i}, \quad (1)$$

where Q_c represents the Q -factor based on the coupling coefficient, and Q_i represents the waveguide loss limited quality factor. The total Q -factor can be expressed as:

$$Q_{\text{total}} = \frac{-2\pi^2 \cdot R \cdot n_g}{\lambda \cdot \ln[\gamma \sqrt{(1 - \kappa_1)(1 - \kappa_2)}]}, \quad (2)$$

where λ is the resonant wavelength, R is the radius of the MRR, n_g is the group index, γ is the amplitude transmission after each roundtrip (equal to $10^{-\alpha L/20}$ in dB per unit length), and κ_1 and κ_2 are the power coupling ratios defined as the amount of power coupled from the input port to the cross port (for all-pass MRRs, $\kappa_2 = 0$). Alternatively, the Q -factor can be approximated by dividing the resonant peak's wavelength by its full width at half maximum:¹⁰

$$Q = \omega \frac{\varepsilon}{\partial \varepsilon / \partial t} = \frac{2\pi \cdot n_g \cdot 4.34}{\lambda \cdot \alpha_{(\text{dB/m})}} \approx \frac{\lambda}{\Delta \lambda_{\text{FWHM}}}, \quad (3)$$

where α is the losses in the resonator, $\omega = 2\pi f$ is the resonance frequency, $\partial \varepsilon / \partial t$ is the mode's energy versus time, and $\Delta \lambda_{\text{FWHM}}$ is the FWHM bandwidth of the resonance peak (or called 3-dB bandwidth).

Another important figure of merit is the extinction ratio (ER). In communications, this value is dictated by the receivers sensitivity for a certain bit error rate (BER).¹³ The ER describes the ratio of the maximum to

minimum powers, either at the through or drop ports transmission. For the all-pass MRR, the maximum power (T_{\max}) occurs off resonance, and minimum power (T_{\min}) occurs on resonance, since most of the power is coupled and trapped inside of the resonator. A concept, critical coupling, describes the condition that the transmission T completely drops to 0 at the output, which occurs when the bus coupled power (κ^2) equals the total round-trip loss ($1 - \gamma^2$) inside the resonator.

To obtain the best performance of the proposed SWG waveguide-based MRR configuration (high Q -factor and high ER), MODE Solutions were introduced for 2D simulations. As presented in Figure 2(a) below, the SWG-based waveguide was replaced with an equivalent 2D uniform waveguide by applying the effective medium theory (EMT) along the propagation direction, where the index of the uniform waveguide is the square root of the volume-weighted average of the square of the refractive index of the sub-wavelength material ($n_{\text{EMT}}^2 = \eta n_{\text{core}}^2 + (1 - \eta)n_{\text{gap}}^2$). The SWG waveguide shows an effective medium with the index of 2.657 and 2.628 for oxide and water claddings. However, due to the fabrication limit, the minimum feature size under air cladding is not less than 400 nm, breaking the Bragg condition at C-band wavelength. Therefore, only designs under the IME-PDK for oxide cladding were submitted. For air/water cladding configurations, an oxide removal post-process by the reactive-ion etching (RIE) system can be carried out later after receiving the chips from IME. By varying the distance between the bus waveguide and MRR, the coupled and transmitted power ratios as a function of wavelengths were obtained from Monitor 1 and Monitor 2, respectively in the VarFDTD Solver (Figure 2(b)), which can save much simulation time compared to 3D-FDTD simulations. In addition, the waveguide propagation loss ($\alpha_{\text{water}} = 28 \text{ dB/cm}$, $\alpha_{\text{oxide}} = 0 \text{ dB/cm}$) and frequency response were generated from MODE Solutions by using Eigenmode Solver. By importing these data into a Matlab-based script, the transmission spectrum as a function of wavelength is obtained based on:

$$T = \frac{I_t}{I_{\text{in}}} = \frac{t^2 + \gamma^2 - 2t\gamma\cos\phi}{1 + t^2\gamma^2 - 2t\gamma\cos\phi}, \quad (4)$$

where t is the through-port coefficient, and ϕ is the phase change after one round trip of the ring ($\phi = 2\pi r\beta$) as well as the FSR ($\text{FSR} = \lambda^2/2\pi r n_g$) and Q -factors. The simulated results are presented in Figure 3 with a radius of 20 μm SWG-based MRR under oxide cladding. The critical coupling ($t = \gamma$) happens when the coupling distance is 300 nm with a Q -factor around 12000 at 1550 nm. Similarly, the best coupling distance for water cladded MRR is 500 nm with an improved Q -factor of 5800 as presented in Figure 3(c) and 3(d).

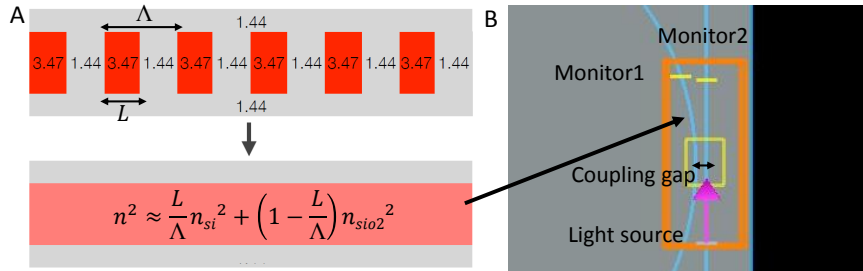


Figure 2: (a) Effective medium theory generated the effective index of a uniform waveguide according to the SWG-based configuration, where $\Lambda = 300 \text{ nm}$, and $\eta = 0.5$. (b) Coupling coefficient simulation by introducing the EMT waveguide into MODE Solutions with a varied coupling distance. Monitor1 is used to detect the coupled power and Monitor2 is used to detect the through power.

4.1.2 Waveguide crossings

Although the waveguide crossing based on the SWG configurations has been reported in 2010 through the EBL fabrication process,¹⁴ in the past 10 years, to the best of our knowledge, this architecture is still not realized by the deep-UV lithography process. In this part, we introduce a waveguide crossing using SWG geometries through the AMF foundry. Based on the minimum feature size of the AMF foundry of 120 nm, our SWG geometry has the period of 240 nm, and the duty cycle of 50%, in the TE mode.

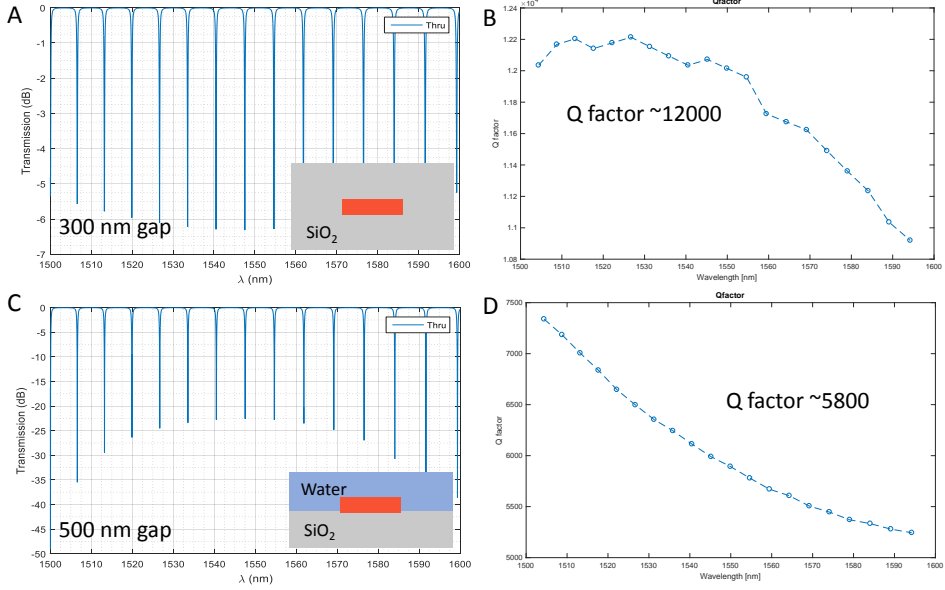


Figure 3: (a) The simulated transmission spectrum of SWG-based MRR with a radius of 20 μm and a coupling distance of 300 nm. The cladding material is oxide. (b) Calculated Q -factors based on the transmission plot, showing a value of around 12000 at 1550 nm wavelengths. (c) The simulated transmission spectrum of SWG-based MRR with a radius of 20 μm and a coupling distance of 500 nm. The cladding material is water. (d) Calculated Q -factors based on the transmission plot, showing a value of around 5800 at 1550 nm wavelengths.

A waveguide intersecting another waveguide (crossing) will lead to a cross-region with no/low lateral mode confinement. Light propagating through the crossing diffracts and causes loss due to the excitation of radiation modes and crosstalk by coupling to the guided modes of the intersecting waveguide.¹⁴ The SWG waveguide shows a lower n_{eff} as compared to the standard strip waveguide, which can extend the mode cross-section. In addition, the effective index property of the SWG waveguide can be tailored by varying parameters of the SWG. Therefore, SWG geometries are very suitable as the mode converter for efficient waveguide crossings, by gradually changing the effective index of the SWG waveguide through chirping the pitch and tapering the width of the grating segments, as shown in Ref. 14. However, in our aspect, since 120 nm is the minimum feature size available for the AMF foundry, only the waveguide wide of the silicon pillar is tunable for the effective index adiabatic transition along the SWG waveguide. By narrowing the width of the silicon pillar from the edge (500 nm) to the center (400 nm) of the crossing, the effective index of the waveguide is gradually reduced.

To reduce the mode mismatch loss in the waveguide crossing, two parts of the crossing need to be finely adjusted in order to ensure a constant effective index variation. The first part is the taper connecting the standard waveguide with the SWG waveguide. As shown in Figure 4(a), by gradually adding the SWG pillar to the taper from the standard waveguide terminal to the SWG waveguide terminal, a sudden index change will occur at the interface between the end of the taper and the beginning of the SWG waveguide when the SWG pillar is constantly the same. To minimize the index bump along the waveguide, we need to change the width of the pillar or the pitch of the SWG. Based on our colleague's work, keeping the period and duty cycle constant is important to decrease the back-reflection in the SWG taper. Therefore, two methods have been applied for the index matching: enlarging the width of the pillar in the SWG part (SWG-enlarged), or reducing the width of the pillar in the taper part (taper-shrunked), presented in Figure 4(a). The effective index of the SWG pillar with different width was simulated by the FDTD bandstructure calculations. Transmission simulations were realized by using MODE Solutions, and the result is depicted in Figure 4(b). It can be observed that both two methods can improve the transmission power through the taper from the standard waveguide to the SWG waveguide, compared to the regular SWG taper.

Another important part is the intersecting in the crossing. As shown in Figure 5 below, the intersecting SWG

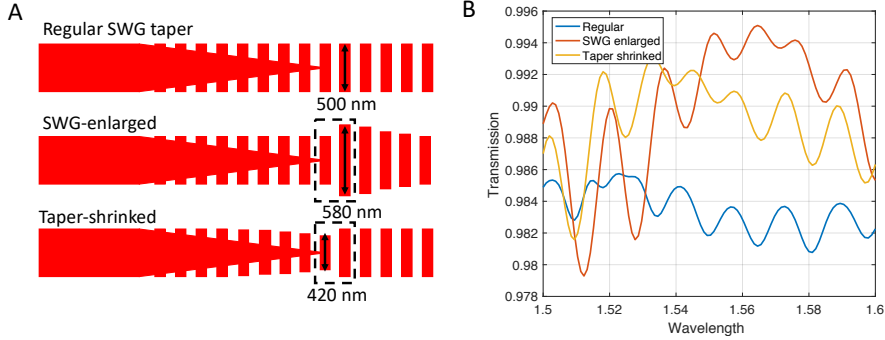


Figure 4: (a) Different SWG taper architectures: regular SWG taper, SWG-enlarged taper, and taper-shrunked taper, from top to bottom, respectively. (b) Transmission spectra of three proposed SWG tapers at the C-band wavelength.

structure has the same grating parameters, except the width, while the center part is $250 \times 250 \text{ nm}^2$ square to ensure an identical geometry for both waveguides. The center segment dimension is set to match the area of the adjacent SWG pillar to maintain a constant effective index for these adjacent segments.

From the FDTD simulation, we found that the effective index of the SWG waveguide ($\Lambda = 240 \text{ nm}$, and $\eta = 50\%$) is 1.638 for the pillar width of 500 nm. However, with the width of SWG pillars narrows down to 400 nm, the effective index will decrease more close to the intersecting area, which may cause a huge substrate leakage due to the absorption of the silicon substrate underneath the buried oxide (BOX) layer. Therefore, a substrate undercut process is required for this SWG-based waveguide crossing, as described in Ref. 15. This process can partially remove the silicon substrate by wet etching and give a symmetric mode profile in the waveguide, thus reducing the substrate leakage losses.

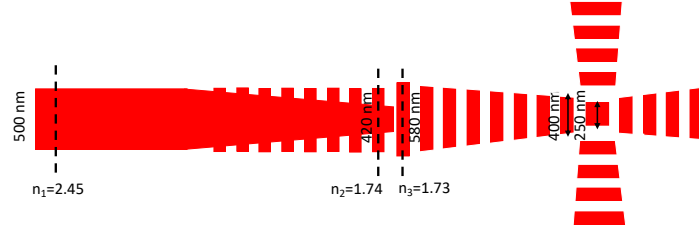


Figure 5: Schematic of the SWG-based waveguide crossing. A $250 \times 250 \text{ nm}^2$ silicon square is placed in the middle of the crossing to ensure the constant effective index variation and reduce the back reflection losses.

4.2 Design layout

The fabrication layout was achieved by using KLayout. KLayout supports several design flows that can be mixed depending on the project enabling a team to collaborate on. The most common approach is to use the graphical user interface (GUI) to design using a library of fixed and parameterized cells (PCells). The SWG waveguide-base MRR PCell is available in the SiEPIC-EBeam-PDK as “SWG_Ring”, offering adjustable parameters including the period (Λ), duty cycle (η), waveguide width (W), ring radius (r), and coupling distance (g), etc.¹⁶ As presented in Figure 6, the proposed SWG-based MRR were designed with different coupling distance from 150 to 900 nm in order to find the critical coupling condition with a radius of 20 μm . The design layout was submitted to IME A*STAR, Singapore and Applied Nanotools (ANT) Int., Canada both for the deep-UV lithography and EBeam lithography, respectively, with the oxide cladding on top.

As for the waveguide crossing, there is no specific PCell yet. Thus, A four-port crossing with the following parameters was designed in order to characterize the transmission and the crosstalk performance: $\Lambda = 240 \text{ nm}$, $\eta = 50\%$, $W_{\text{SWG}} = 500\text{--}400 \text{ nm}$, and $W_{\text{center}} = 250 \text{ nm}$ (as shown in Figure 7). In addition, plenty of cascaded

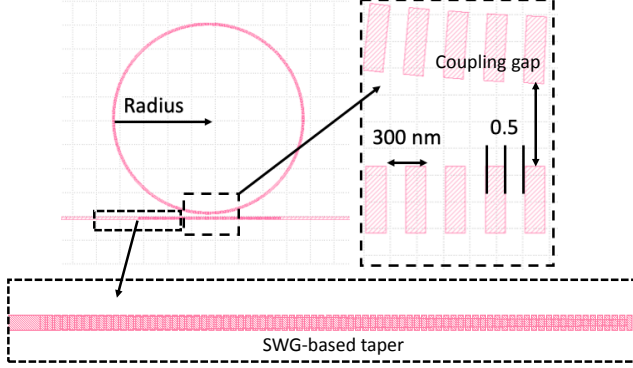


Figure 6: The SWG waveguide-based MRR layout generated by using PCell “SWG_Ring” with a period of 300 nm, duty cycle of 0.5, waveguide width of 500 nm, radius of 20 μm , and varied coupling distance. A 10- μm -long SWG-based taper is used to smoothly convert the standard 500 \times 220 nm waveguide to the SWG waveguide.

SWG-based crossings were also designed for the cut-back measurement to calculate the insertion losses. The design layout was submitted to AMF, Singapore for fabrication.

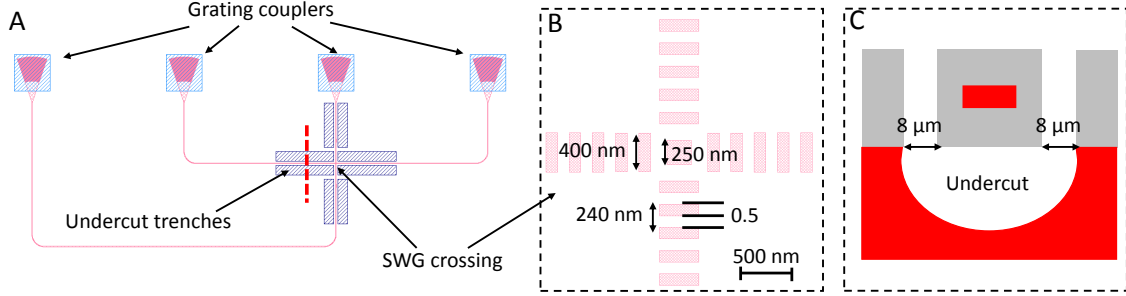


Figure 7: (a) The four-port SWG-based waveguide crossing test structure. (b) Zoom-in image of the crossing region. (c) Cross-section of the substrate undercut waveguide, where the silicon layer is isotropically etched through the 8 μm wide oxide trenches on both sides of the waveguide.

To investigate the propagation losses of the SWG waveguide and the insertion losses of the SWG taper, we also designed plenty of cut-back SWG-waveguide-based symmetric MZI architectures and head-to-head cascaded SWG tapers, respectively. For the group index and the propagation losses of the SWG waveguide, we can calculate based on the following equations:¹⁷

$$\Delta n_g = \frac{\lambda_{\max} \lambda_{\min}}{2L_{\text{arm}}(\lambda_{\max} - \lambda_{\min})} = n_g^{\text{WG}} - n_g^{\text{SWG}}, \quad (5)$$

$$\Delta \alpha = \frac{1}{L_{\text{arm}}[\text{cm}]} \left[20 \log \left(\frac{10^{R/20} + 1}{10^{R/20} - 1} \right) \right] [\text{dB/cm}] = \alpha^{\text{WG}} - (\alpha^{\text{SWG}} + \alpha^{\text{taper}}), \quad (6)$$

where L_{arm} is the length of the symmetric MZI arm, R is the difference between the maximum and the minimum transmittance, λ_{\max} and λ_{\min} are the wavelength of maximum and minimum powers of the transmission spectrum, n_g^{WG} and n_g^{SWG} are the group index of the standard and SWG waveguides, and α^{WG} , α^{SWG} and α^{taper} are the loss per unit length of standard and SWG waveguides and loss per SWG taper, respectively.

5. METHOD AND MEASUREMENT

5.1 Experimental setup

Optical characterizations were carried out by using a custom silicon photonic test setup and software controlled by a Windows PC. A tunable laser (Agilent 81600B) and power detectors (Agilent 81635A) were employed as the tunable optical source and readout. An eight-port polarization maintaining fiber-array with four-TE and four-TM polarized ports, respectively, (PLC Connections, Columbus, OH) was connected to the lightwave mainframe to couple the light on and off the silicon chip. The silicon chip was placed on an aluminum stage thermally controlled by a temperature controller during the optical measurements (LDC501, Stanford Research Systems), and held by a vacuum system.

5.2 IME-based SWG microrings

5.2.1 Fabrication results

The optical measured results of SWG-MRRs are presented in Figure 8(a) and 8(b) below by sweeping the tunable laser with a resolution of 0.01 nm. From these transmission plots, a Q -factor of 457, maximum ER of 42.3 dB, and FSR of 7.11 nm are observed for the IME deep-UV lithography process; and a Q -factor of 3456, maximum ER of 30.5 dB, and FSR of 7.03 nm are observed for the ANT Ebeam-litho process. Based on the FSR values, the group indices of both SWG-based MRR are achieved, with 2.52 and 2.70 for the IME and ANT-based processes at 1500 nm and 1550 nm, respectively. It is obvious to draw the conclusion that the SWG-based MRR device from the IME foundry suffers huge propagation losses due to the deep-UV fabrication issues, including the radiation losses and substrate leakage caused by the enlarged optical mode, side-wall roughness scattering losses, and bend radiation and reflection losses. To characterize the total internal losses from the MRR device,

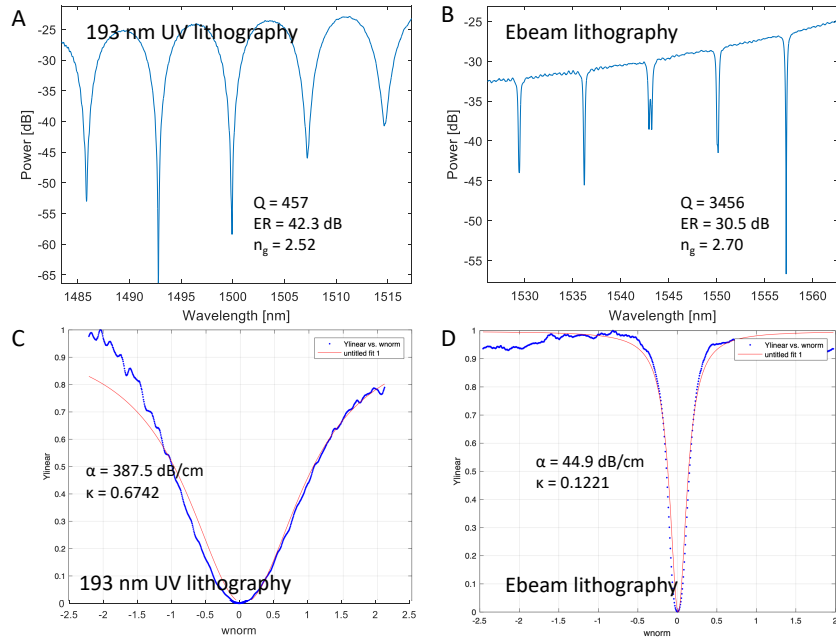


Figure 8: (a) Transmission spectrum of the proposed SWG-based MRR fabricated by IME 193 nm deep-UV lithography process, depicting a Q -factor of 457 and ER of 42.3 dB. (b) Transmission spectrum of the proposed SWG-based MRR fabricated by ANT Ebeam-lithography process, depicting a Q -factor of 3456 and ER of 30.5 dB. (c) Lorentzian curve fitted resonant peak (red curve) of the IME foundry-based SWG MRR, indicating a loss of 388 dB/cm. (d) Lorentzian curve fitted resonant peak (red curve) of the ANT foundry-based SWG MRR, indicating a loss of 45 dB/cm.

another Matlab script was introduced for the Lorentzian curve fitting of the resonator's transmission, which is

based on the coupled-mode theory (CMT). The through port transmission is expressed as Equation 4. Then, we can obtain the Lorentzian function for the all-pass MRR ($\kappa_2 = 0$, $c_2 = 1$) through port transmission:

$$Y_{linear} = \frac{((1 - \kappa) - 2\sqrt{(1 - \kappa)}\gamma \cos(\omega_{norm} - \phi) + \gamma^2)}{(1 - 2\sqrt{(1 - \kappa)}\gamma \cos(\omega_{norm} - \phi) + (1 - \kappa)\gamma^2)}, \quad (7)$$

where ω_{norm} is the normalized phase, which is calculated by dividing the wavelength by the FSR (in wavelength). As presented in Figure 8(c) and 8(d), the propagation losses and the power coupling ratio have been obtained through the Lorentzian fitting function. For the UV-lithography-based MRR, $\alpha = 387.5$ dB/cm with $\kappa = 0.674$; for the Ebeam-litho MRR, $\alpha = 44.8$ dB/cm with $\kappa = 0.122$. Therefore, it is of great importance to figure out where the losses are generated from and how to improve the performance based on the fabrication limitations of CMOS processes.

Since there are no available SEM images for the SWG configurations from IME foundry-based deep-UV lithography process, to characterize the fabrication results with the feature size around 150 nm, we introduced a custom litho-simulation software, which generates multiple batches of calibration pattern arrays through IME-based fabrications. Figure 9 gives the layout of the proposed SWG configurations with (green blocks) and without (pink blocks) the litho simulation. It is obvious to see that after the litho simulation, the 150×500 nm² silicon block is shrunk to a 174×455 nm² capsule, which may explain the decreased group index in Figure 8(a). Furthermore, the coupling distance between the ring and bus waveguide is also influenced, rendering a 50-nm-wider gap compared to the designed one.

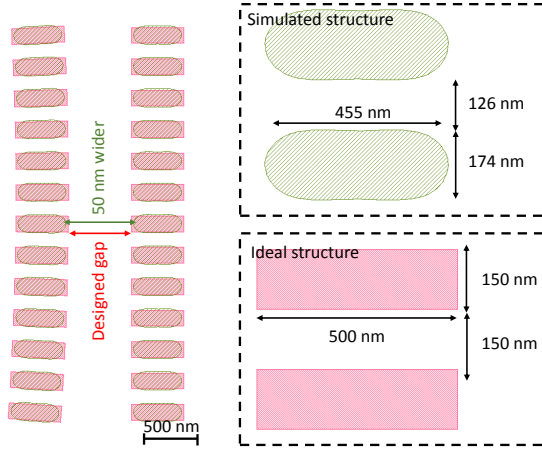


Figure 9: The proposed SWG-based MRR configuration with 150×500 nm² silicon block in optimum (pink pattern), and with 174×455 nm² block in litho-simulation (green pattern). The coupling distance is 50 nm wider compared to the designed gap.

5.2.2 Configuration optimization

MODE and FDTD Solutions were used again for the optimization of the proposed SWG configuration after litho-simulation. By importing the layout file directly into MODE Solutions, the capsule-like SWG MRR configuration with single bus-waveguide was characterized under the VarFDTD Solver. A fundamental TE mode-based light source was employed to shine the input port, and a 2D monitor was used to image the mode propagation in the SWG MRR. The simulation results are depicted in Figure 10(a) and 10(b), showing that most of the light has been dismissed due to the bend radiation and scattering losses. The transmission plot was also obtained from the simulation, showing a Q -factor of 2970, higher than the measured result, indicating a more complex loss mechanism in the proposed SWG MRR. That may be due to the worse configuration of fabricated SWG through CMOS processes or the ultra high side-wall scattering losses. In addition, by using FDTD band structure calculations simulation for the capsule-like SWG waveguides, a n_{eff} of 1.64, and n_g of 2.53 are obtained at 1550

nm, indicating a low optical confinement of the guided mode; thus a higher mode size interacting with the side-walls, and substrate material leakage (Figure 10(c) and 10(d)). Compared to the measured group index in Figure 8(a), the simulated group index of the litho-simulated capsule-like SWG pillar does not match well with a discrepancy of 0.15 ($n_{g(\text{simu})} = 2.67$ in Figure 10(d)) at 1500 nm. Several methods are needed to improve the optical performance of the proposed SWG-based MRR devices: 1. Enlarging the radius of the ring, which can effectively decrease the radiation losses; 2. Increasing the weight ratio of Si in the SWG waveguide to increase the index values in order to reduce the leakage losses; 3. Using the asymmetric silicon pillars for the ring resonator part, which can confine the optical mode close to the inner side of the waveguide, to reduce the back-scattering and radiation losses.

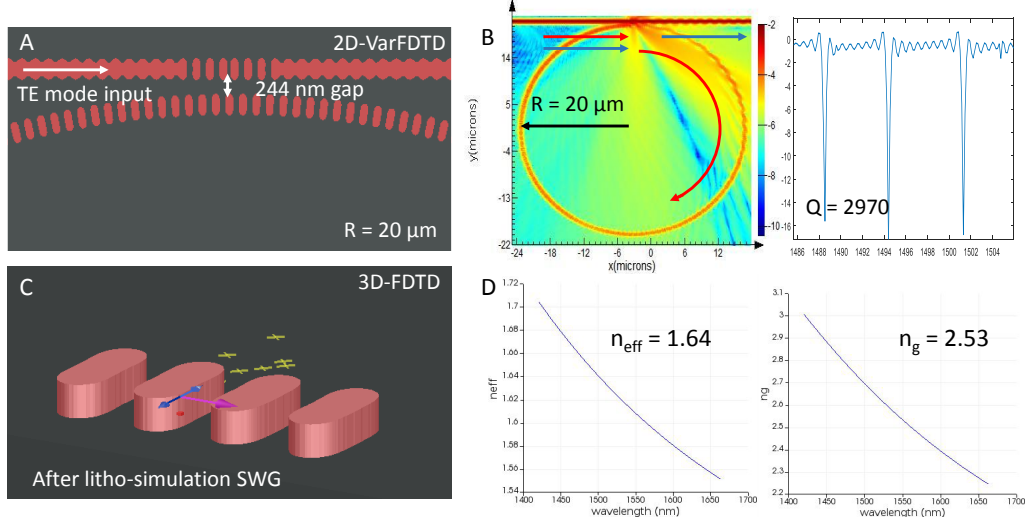


Figure 10: (a) The imported capsule-like SWG-based MRR layout in MODE Solutions after litho-simulation. The coupling distance is around 244 nm, compared to the original one of 200 nm. The radius is set to 20 μm . (b) Left: The top-view of a power monitor on the entire MRR (color-bar is in the unit of the decibel), showing huge losses at the coupling region and SWG bends. Right: The transmission plot of the proposed MRR through 2D VarFDTD simulation. (c) FDTD band structure simulation with the capsule-like SWG pillars. (d) The simulated effective and group indices are 1.64 and 2.53, respectively, at 1550 nm wavelengths.

Recently, a Q -factor highly-improved SWG-based MRR configuration has been reported by introducing trapezoidal silicon pillars, which can reduce the bend loss by creating an asymmetric effective refractive index profile in the MRR (as shown in Figure 11(a)), yielding a Q -factor as high as 11500 with a radius of 5 m, 4.6 times of that (~ 2800) offered by a conventional SWG through EBL processes.¹⁸ By utilizing a trapezoidal-shaped SWG core, an enhanced sensing capability was analyzed and characterized, obtaining a high Q -factor of 9100, bulk sensitivity of 440.5 nm/RIU and surface sensitivity of 1 nm/nm.¹⁹ Therefore, to improve the Q -factor of CMOS-based SWG MRRs, we employed the concept of trapezoidal silicon blocks to our configurations. By applying the conformal transformation method, which transforms the effective index profile conformally, a bend SWG waveguide can be taken equivalently as a straight SWG waveguide with a transformed Cartesian coordinate system as depicted in Figure 11(b). The first order approximation of transformed effective refractive index can be expressed as:²⁰

$$n_{\text{eff}}(r) = \begin{cases} n_{\text{clad}} & r < r_1, r > r_2 \\ n_{\text{core}} & r_1 \leq r \leq r_2, \end{cases} \quad (8)$$

and the conformally transformed index value:

$$n_{\text{con}}(u) = n_{\text{eff}}(r_2 e^{u/r_2}) e^{u/r_2}, \quad (9)$$

and

$$u = -r_2 \ln \frac{r_2}{r}, \quad (10)$$

where r is the position of the cross-section of the waveguide. Therefore, by introducing the geometric parameters from the published designs,¹⁸ a trapezoidal-shaped SWG configuration is achieved in Figure 11(c) below. The top-views of the power transmission in the 90° bend consisting of the capsule-like and trapezoidal-shaped SWG pillars are shown in Figure 11(d). The left one is the standard SWG bend with the litho-simulation process applied, and the radius is 20 μm . For the right one, we enlarged the radius to 30 μm and used the trapezoidal-shaped SWG (T-SWG) instead, indicating a low power loss during the light propagating inside the bend part. However, the interface between the SWG-taper to the bend SWG waveguide is not optimized, that explains the huge mode-mismatch observed in Figure 11(d).

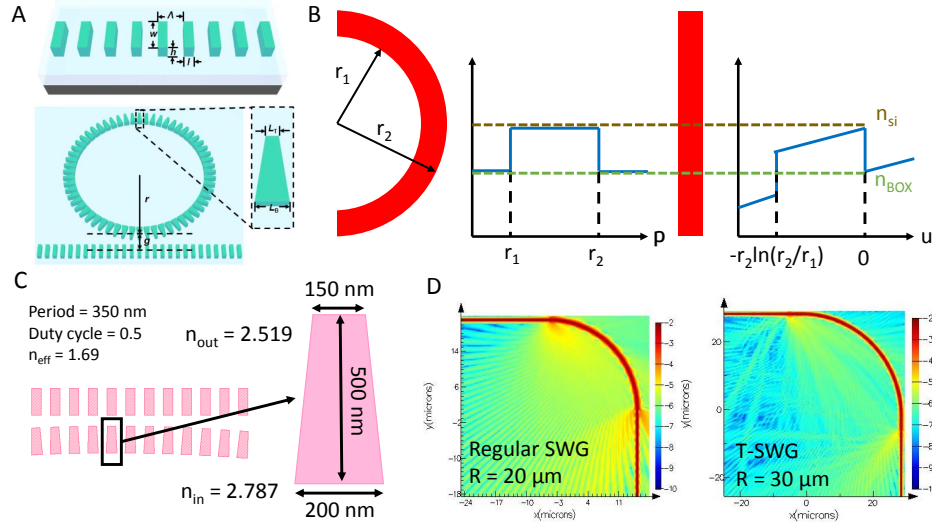


Figure 11: (a) 3D schematic of a standard SWG waveguide and a trapezoidal-shaped SWG waveguide.¹⁸ (b) Standard bend waveguide refractive index profile, and conformal transformation method applied refractive index profile corresponding a straight waveguide. Most of the optical mode is confined at the outer side of the bend, thus the inner part index shows a decreased value. (c) The designed trapezoidal-shaped SWG pillar for MRR configuration, with an effective index around 1.70. (d) VarFDTD simulation-based transmission top-views in the decibel unit of a regular 90° bend SWG waveguide after litho-simulation and T-shaped optimization. The radii are 20 and 30 μm for capsule-SWG and T-SWG, respectively.

5.2.3 Performance validation

To characterize optical performance of the optimized trapezoidal-shaped SWG configurations, several types of SWG-based MRR were designed and submitted to EBL processes for fabrication (presented in Figure 12(a)), including: standard SWG with 300 nm period and 0.5 duty cycle; litho-simulated standard SWG; T-shaped SWG with 350 nm period and 0.5 duty cycle (mean value); and litho-simulated T-shaped SWG. The T-shape SWG configuration is also realized via the PCell “SWG_Ring”, where the width ratio ($L_{\text{in}}/L_{\text{out}}$) of inner and outer sides of the Si block can be adjusted for a trapezoidal shape. All MRR configurations were coupled with single SWG-based bus waveguide under varied coupling distance, with the radius of 20 μm for std-SWG and litho-simulated std-SWG MRRs, and 30 μm for T-SWG and litho-simulated T-SWG MRRs. SEM images are also depicted below in Figure 12(b), as well as their transmission spectra in Figure 12(c), respectively. By measuring the full width at half maximum (FWHM) of these resonant peaks from each SWG MRR configuration, the Q -factor is calculated based on Equation 3, indicating $Q_{\text{std-SWG}} = 3740$, $Q_{\text{litho-SWG}} = 1092$, $Q_{\text{T-SWG}} = 11207$, and $Q_{\text{litho-TSWG}} = 10427$, respectively. However, it is worth to inform that for T-shape SWG MRRs, their radius is 30 μm , larger than the standard SWG MRRs (20 μm), which should also improve the Q -factor because of the minimized the bend radiation loss.

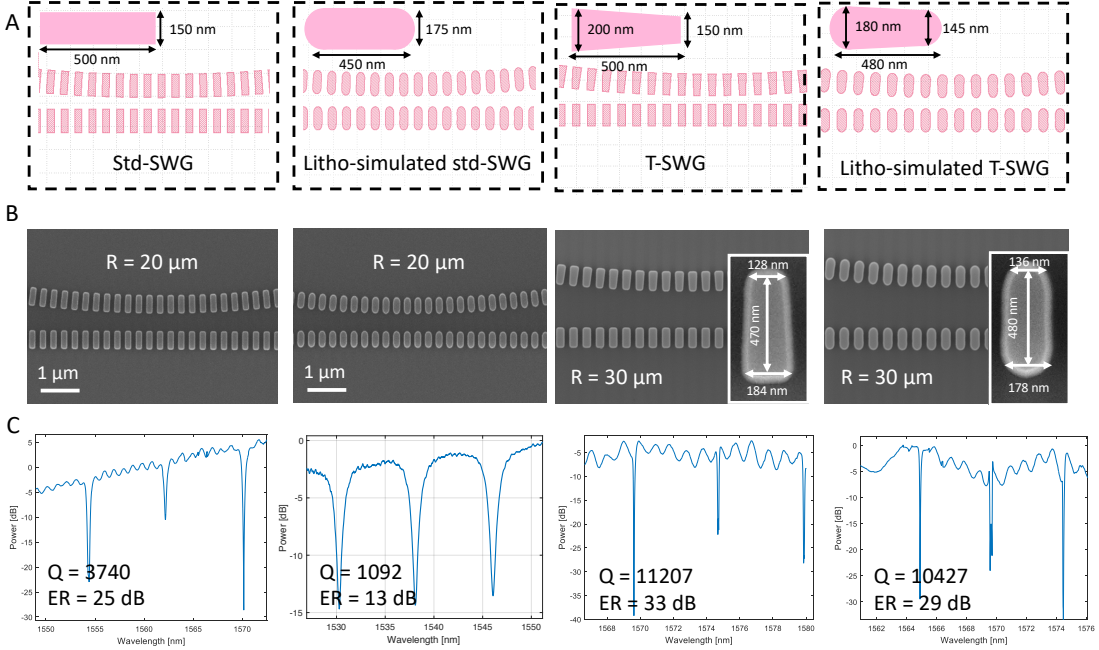


Figure 12: (a) Layout images of the proposed std-SWG, litho-simulated std-SWG, T-SWG, and litho-simulated T-SWG MRRs, respectively. (b) SEM images of these SWG MRR configurations. (c) Transmission spectra of these SWE MRR configurations.

5.3 AMF-based SWG waveguide crossings

For the SWG configuration manufactured by the AMF foundry, to facilitate subsequent SEM imaging, we also placed the SWG waveguide onto a 90-nm rib with the oxide cladding removed. Figure 13 shows the SEM image of SWG pillars fabricated on the rib by the AMF foundry. Although it cannot be completely represented the SWG on the strip waveguide, the rib-SWG waveguide still can depict the effect of the deep-UV lithography for small-feature-size architectures. Due to the overexposure, the SWG pillar shows a capsule-like shape, similar to the aforementioned litho-simulation result, but even worse to maintain the rectangle shape, which may be due to the smaller feature size of 120 nm. This SWG configuration may lead to a lower effective index compared to the FDTD simulations, and generate more losses. Real SEM imaging on the 220-nm-thick SWG block is still needed to be studied, which will be carried out by using the HF-based wet etching to remove the cladding at the University of British Columbia.

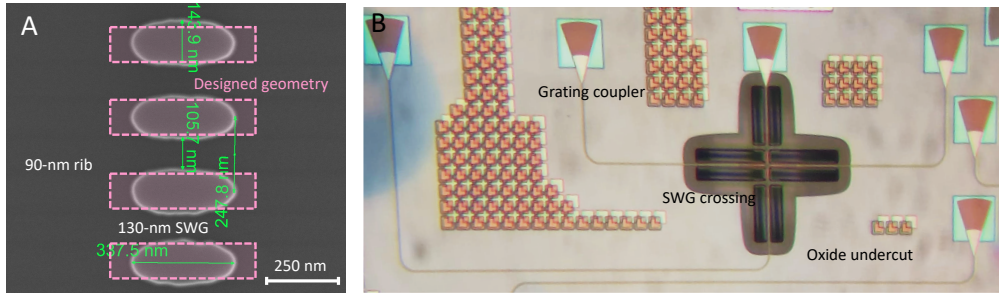


Figure 13: (a) SEM image of the SWG pillar on a 90-nm rib layer. The pink rectangles represent the designed SWG geometry with $\Lambda = 240$ nm, and $\eta = 50\%$. (b) Microscopic image of the SWG-based waveguide crossing, with silicon substrate undercut process.

The performance of the SWG-based waveguide crossing was also characterized. Two important parameters, the insertion loss and the crosstalk were measured based on the cut-back cascaded SWG crossings and a single four-port SWG crossing, respectively. As shown in Figure 14(a), transmission spectra for the cut-back SWG crossings architectures are presented as a function of the wavelength, from 0, 1, 7, and 14 cascaded SWG crossings, respectively. The mean insertion loss of each SWG crossing is presented in Figure 14(b), indicating the IL = ~ 2.3 dB/crossing. To characterize the crosstalk, we injected the light through the port-1 and port-2 of the single SWG crossing, respectively, and detected transmission powers from the rest three ports. Figure 14(c) and 14(d) depict the transmission spectra, showing a crosstalk larger 40 dB.

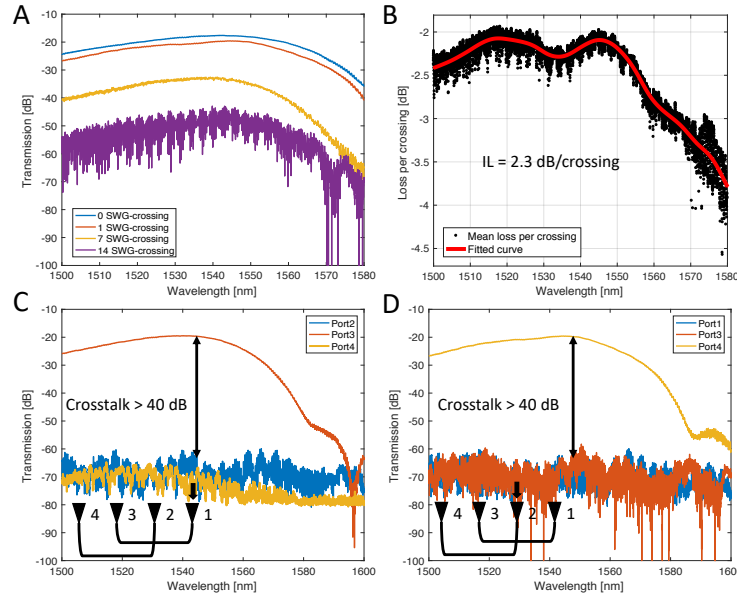


Figure 14: (a) Transmission spectra of the cascaded SWG crossings with the crossing number of 0, 1, 7, and 14, respectively. (b) Mean insertion loss per crossing according to the cut-back SWG crossings as a function of wavelength, showing a 2.3 dB/crossing at 1550 nm. (c) The transmission plot of a single SWG crossing with the input at port-1. (d) The transmission plot of a single SWG crossing with the input at port-2.

The insertion loss is almost 100 times higher than the previously published SWG crossing based on the EBL process,¹⁴ thus, it is important to evaluate the main sources of the loss. Two potential loss source exist in the proposed SWG crossing: the scattering losses and the substrate absorption losses. To figure out which loss is dominant, we also designed a series of cut-back SWG waveguides-based MZIs (one arm of std-waveguide, and one-arm of SWG-waveguide), with no undercut processes. By measuring these symmetric MZIs, the group index and the propagation loss of the SWG waveguide can be calculated according to the Equations 5 and 6. Figure 15(a) below shows the transmission spectrum of the symmetric MZI architecture with an arm length of 1 mm. One of the arms consists of a row of SWG configurations with the pitch of 240 nm, and the duty cycle of 50%. From the obtained R of an average value of 18 dB, and λ_{\max} of 1559.81 nm and λ_{\min} of 1558.67 nm, respectively, we can obtain a Δn_g of 2.38 and a $\Delta \alpha$ of 22 dB/cm. The group index of a standard strip waveguide is estimated to be 4.2, thus the n_g^{SWG} should be around 1.82. It is important to notice that the SWG tapers also generate insertion losses. Therefore, to obtain the insertion loss of the SWG taper (α^{taper}), a series of head-to-head cascaded SWG tapers were measured, and the insertion loss per taper pair is presented in Figure 15(b) versus different SWG geometries. For the Si/gap of 120/120 SWG pillars, the insertion loss is roughly 1 dB/pair. Based on previous measurements, the propagation loss for a standard strip waveguide is ~ 2.5 dB/cm in the TE mode. Therefore, we can calculate the propagation loss of the SWG waveguide is 37 dB/cm.

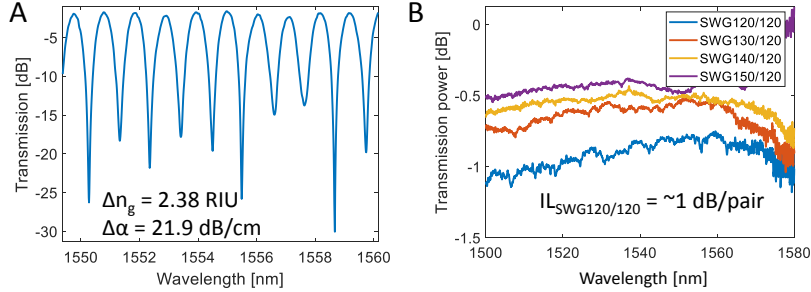


Figure 15: (a) Transmission spectrum of the 1- μm -long symmetric MZI architecture. One of the MZI arms consists of SWG pillars with $\Lambda = 240$ nm, and $\eta = 50\%$, and the other arm is the standard strip waveguide. (b) Insertion loss of the SWG taper-pair with different geometry parameters as a function of the wavelength. The Si/gap is 120/120, 130/120, 140/120, and 150/120, respectively. The IL of the 120/120 SWG is roughly 1 dB/pair.

6. CONCLUSION

In this report, we have designed and characterized the sub-wavelength grating-based configurations fabricated through the deep-UV lithography process. The proposed SWG devices were manufactured through the multi-project wafer service by two foundries: IME and AMF. Due to their different manufacturing processes, the minimum feature size is 180 nm, and 120 nm, respectively, which makes it challenging to fabricate sub-wavelength geometries. We first characterized the optical performance of the SWG MRRs fabricated by IME ($\Lambda = 300$ nm), with a gap distance of 150 nm, a little bit violate the rule. Transmission spectra show the Q -factor 450, roughly 8 times smaller than the SWG MRR fabricated through EBL. Unfortunately, the chip was coated with 2 μm oxide cladding before we received it, which makes it impossible to image the SWG geometry by the SEM system. A custom litho-simulation software, which generates multiple batches of calibration pattern arrays through IME-based fabrications, is applied to simulate the IME foundry fabrication results, which shows a capsule-like silicon pillar with the width of 455 nm, and the length of 174 nm. To improve the Q -factor, we employed the recently published trapezoidal-shape SWG configuration to the MRR. To mimic the IME fabrication effect, the T-shape SWG went through the litho-simulation and fabricated by the EBL process. Experimental results indicate that the Q -factor reaches 10400 for the T-shape SWG MRR with a radius of 30 μm , which provides the potential to fabricate SWG MRR architectures through deep-UV lithography processes. As for the AMF foundry, due to its achievable substrate undercut process and smaller feature size, we designed several SWG-based waveguide crossings, as well as test structures to characterize the propagation losses and the insertion losses of the SWG waveguide and tapers, respectively. The SWG-based waveguide crossing show an insertion loss of 2.3 dB/crossing with a low crosstalk of -40 dB. By extracting from the one-SWG-arm-based symmetric MZI architecture, we obtained the group index and the propagation loss of the SWG waveguide fabricated through AMF foundry, which are 1.82 for n_g^{SWG} and 37 dB/cm for the SWG with the geometry parameters of $\Lambda = 240$ nm, and $\eta = 50\%$. From the SEM image focused on the SWG geometry fabricated on the 90-nm slab, a capsule-like silicon pillar is observed but worse than the litho-simulation predicted, with a width of only 340 nm and rounded edges. This SWG geometry has a lower effective index, which induces a higher substrate leakage, and more portion of the light suffers the side-wall roughness and generate more back-scattering. These may explain the high propagation losses of the SWG waveguide. Future work will focus on enlarging the width of the SWG and narrowing the length before fabrication to compensate for the fabrication effect, i.e. updating the litho-simulation software for the AMF foundry for a fabrication prediction.

7. FOLLOW UPS

Recently we received passive chips based on our latest submitted design from AMF, which do not have any top oxide covering the waveguides. By imaging with SEM, the SWG configuration with a full etch has been displayed. As presented in Figure 16 below, SWG pillars show a capsule-like shape as the litho-simulation software predicted. However, the width of the pillar is ~ 128 nm, which is smaller than the predicted one (174 nm) and the designed one (150 nm). We also imaged the T-shape SWG pillar fabricated by deep-UV lithography

processes, showing $L_{\text{top}} = 114$ nm, and $L_{\text{bot}} = 173$ nm, respectively (the designed top and bottom lengths are 150 and 200 nm). In addition, same SWG configurations were also realized on EBL processes, and SEM images are depicted in Figure 16(c). Compared to the deep-UV lithography, EBL based processes offer more precise fabrication on SWG configurations. However, the round corner issue still remains.

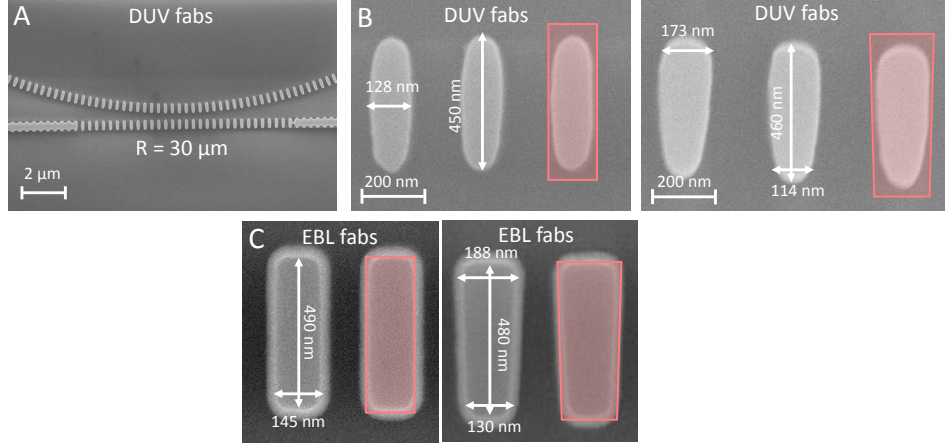


Figure 16: (a) SEM image of the SWG based MRR by deep-UV litho processes. (b) Zoom-in SEM images of SWG pillars by deep-UV litho processes: (left) standard SWG pillars with $\Lambda = 300$ and $\eta = 50\%$, (right) T-shape SWG pillars with $\Lambda = 350$, $\eta = 50\%$ and $L_{\text{top}} = 150$ nm, $L_{\text{bot}} = 200$ nm, respectively. (c) Same SWG configurations fabricated by EBL processes: (left) standard SWG pillars, (right) T-shape SWG pillars.

Due to the low fabrication performance of the SWG configurations by using deep-UV lithography, no resonant peaks were measured of these SWG-based MRRs with water cladded.

8. ACKNOWLEDGEMENTS

The author would like to thank the NSERC CREATE Silicon Electronic Photonic Integrated Circuits (SiEPIC) program and CMC Microsystems for holding passive workshop and enabling the chip fabrication. The author also would like to thank Lumerical, Inc., for the simulation software, M. Kofferleins KLayout for the layout tool, and Institute of Microelectronics (IME), Inc., and Advanced Micro Foundry (AMF), Inc., for chip fabrication. The author would like to appreciate all the instructors during the workshop. The author appreciates the help of Hossam Shoman and Stephen Lin for sharing the Lorentzian curve fitting model and deep-UV lithography simulation model.

REFERENCES

- [1] Laplatine, L., Al'Mrayat, O., Luan, E., Fang, C., Rezaiezadeh, S., Ratner, D., Cheung, K., Dattner, Y., and Chrostowski, L., "System-level integration of active silicon photonic biosensors," in [*Microfluidics, BioMEMS, and Medical Microsystems XV*], **10061**, 100610I, International Society for Optics and Photonics (2017).
- [2] Cheben, P., Xu, D.-X., Janz, S., and Densmore, A., "Subwavelength waveguide grating for mode conversion and light coupling in integrated optics," *Optics express* **14**(11), 4695–4702 (2006).
- [3] Weissman, Z. and Hendel, I., "Analysis of periodically segmented waveguide mode expanders," *Journal of lightwave technology* **13**(10), 2053–2058 (1995).
- [4] Cheben, P., Schmid, J. H., Wang, S., Xu, D.-X., Vachon, M., Janz, S., Lapointe, J., Painchaud, Y., and Picard, M.-J., "Broadband polarization independent nanophotonic coupler for silicon waveguides with ultra-high efficiency," *Optics express* **23**(17), 22553–22563 (2015).
- [5] Benedikovic, D., Cheben, P., Schmid, J. H., Xu, D.-X., Lamontagne, B., Wang, S., Lapointe, J., Halir, R., Ortega-Moñux, A., Janz, S., et al., "Subwavelength index engineered surface grating coupler with sub-decibel efficiency for 220-nm silicon-on-insulator waveguides," *Optics express* **23**(17), 22628–22635 (2015).

- [6] Liu, L., Deng, Q., and Zhou, Z., “Subwavelength-grating-assisted broadband polarization-independent directional coupler,” *Optics letters* **41**(7), 1648–1651 (2016).
- [7] Wangüemert-Pérez, J. G., Cheben, P., Ortega-Moñux, A., Alonso-Ramos, C., Pérez-Galacho, D., Halir, R., Molina-Fernández, I., Xu, D.-X., and Schmid, J. H., “Evanescent field waveguide sensing with subwavelength grating structures in silicon-on-insulator,” *Optics letters* **39**(15), 4442–4445 (2014).
- [8] Flueckiger, J., Schmidt, S., Donzella, V., Sherwali, A., Ratner, D. M., Chrostowski, L., and Cheung, K. C., “Sub-wavelength grating for enhanced ring resonator biosensor,” *Optics express* **24**(14), 15672–15686 (2016).
- [9] Wang, X., Wang, Y., Flueckiger, J., Bojko, R., Liu, A., Reid, A., Pond, J., Jaeger, N. A., and Chrostowski, L., “Precise control of the coupling coefficient through destructive interference in silicon waveguide bragg gratings,” *Optics letters* **39**(19), 5519–5522 (2014).
- [10] Chrostowski, L., Grist, S., Flueckiger, J., Shi, W., Wang, X., Ouellet, E., Yun, H., Webb, M., Nie, B., Liang, Z., et al., “Silicon photonic resonator sensors and devices,” in [*Laser Resonators, Microresonators, and Beam Control XIV*], **8236**, 823620, International Society for Optics and Photonics (2012).
- [11] Alferness, R., Joyner, C., Divino, M., Martyak, M., and Buhl, L., “Narrowband grating resonator filters in ingaasp/imp waveguides,” *Applied physics letters* **49**(3), 125–127 (1986).
- [12] Schmidt, S., Flueckiger, J., Wu, W., Grist, S. M., Fard, S. T., Donzella, V., Khumwan, P., Thompson, E. R., Wang, Q., Kulik, P., et al., “Improving the performance of silicon photonic rings, disks, and bragg gratings for use in label-free biosensing,” in [*Biosensing and Nanomedicine VII*], **9166**, 91660M, International Society for Optics and Photonics (2014).
- [13] Säckinger, E., [*Broadband circuits for optical fiber communication*], John Wiley & Sons (2005).
- [14] Bock, P. J., Cheben, P., Schmid, J. H., Lapointe, J., Delâge, A., Xu, D.-X., Janz, S., Densmore, A., and Hall, T. J., “Subwavelength grating crossings for silicon wire waveguides,” *Optics express* **18**(15), 16146–16155 (2010).
- [15] Lu, Z., Murray, K., Jayatilleka, H., and Chrostowski, L., “Michelson interferometer thermo-optic switch on soi with a 50- μ w power consumption,” *IEEE Photonics Technology Letters* **27**(22), 2319–2322 (2015).
- [16] “SiEPIC-EBeam-PDK package for KLayout.” https://github.com/lukasc-ubc/SiEPIC_EBeam_PDK. Accessed: 2018-11-30.
- [17] Sarmiento-Merenguel, J. D., Ortega-Moñux, A., Fédéli, J.-M., Wangüemert-Pérez, J. G., Alonso-Ramos, C., Durán-Valdeiglesias, E., Cheben, P., Molina-Fernández, I., and Halir, R., “Controlling leakage losses in subwavelength grating silicon metamaterial waveguides,” *Optics letters* **41**(15), 3443–3446 (2016).
- [18] Wang, Z., Xu, X., Fan, D., Wang, Y., and Chen, R. T., “High quality factor subwavelength grating waveguide micro-ring resonator based on trapezoidal silicon pillars,” *Optics letters* **41**(14), 3375–3378 (2016).
- [19] Yan, H., Huang, L., Xu, X., Chakravarty, S., Tang, N., Tian, H., and Chen, R. T., “Unique surface sensing property and enhanced sensitivity in microring resonator biosensors based on subwavelength grating waveguides,” *Optics express* **24**(26), 29724–29733 (2016).
- [20] Smit, M. K., Pennings, E. C., and Blok, H., “A normalized approach to the design of low-loss optical waveguide bends,” *Journal of lightwave technology* **11**(11), 1737–1742 (1993).